Widefield microwave imaging in alkali vapor cells with sub-100 m resolution

New Journal of Physics

The open access journal at the forefront of physics

CrossMark

FAST TRACK COMMUNICATION

Widefield microwave imaging in alkali vapor cells with sub-100 μm resolution

Andrew Horsley, Guan-Xiang Du and Philipp Treutlein

Departement Physik, Universität Basel, Switzerland

**E-mail:** andrew.horsley@unibas.ch and philipp.treutlein@unibas.ch

Abstract

We report on widefield microwave vector field imaging with sub-100 μm resolution using a microfabricated alkali vapor cell. The setup can additionally image dc magnetic fields, and can be configured to image microwave electric fields. Our camera-based widefield imaging system records 2D images with a 6×6 mm^2 field of view at a rate of 10 Hz. It provides up to 50 μm spatial resolution, and allows imaging of fields as close as 150 μm above structures, through the use of thin external cell walls. This is crucial in allowing us to take practical advantage of the high spatial resolution, as feature sizes in near-fields are on the order of the distance from their source, and represent an order of magnitude improvement in surface-feature resolution compared to previous vapor cell experiments. We present microwave and dc magnetic field images above a selection of devices, demonstrating a microwave sensitivity of 1.4 μT Hz$^{-1/2}$ per $50 \times 50 \times 140$ μm^3 voxel, at present limited by the speed of our camera system. Since we image 120×120 voxels in parallel, a single scanned sensor would require a sensitivity of at least 12 nT Hz$^{-1/2}$ to produce images with the same sensitivity. Our technique could prove transformative in the design, characterization, and debugging of microwave devices, as there are currently no satisfactory established microwave imaging techniques. Moreover, it could find applications in medical imaging.

1. Introduction

Atomic vapor cells are one of the most versatile systems for measuring electromagnetic fields [1–3], and are at the heart of the most sensitive dc [4, 5] and rf [6, 7] magnetometers. Our group has recently developed a technique for imaging magnetic fields at microwave frequencies [8–10], and alkali atoms in Rydberg states have been used for imaging microwave electric fields [11–14]. These techniques promise to have a transformative effect on the development, function and failure analysis of microwave devices in science and industry, as there is currently no established and satisfactory technique for imaging microwave fields. There is also significant interest in microwave sensing and imaging for medical applications, such as breast cancer screening [15–17]. However, while providing high field sensitivity, current vapor cell devices are limited to an exploitable spatial resolution on the millimeter scale.

Here we report a new setup based on a 140 μm 'ultrathin' vapor cell for high-resolution imaging, providing $50 \times 50 \times 140$ μm^3 spatial resolution in the cell bulk, and allowing us to image fields as close as 150 μm above surfaces, thanks to a thin external wall. This represents an order of magnitude improvement in exploitable spatial resolution compared to previous vapor cell experiments, and allows us to enter the relevant regime for imaging fields of industrial microwave devices. Our camera-based imaging technique allows us to record widefield 2D images at a rate of 10 Hz, which could be further improved to kHz rates using a faster camera system [18]. This allows us to record live movies of time-dependent processes, which would be rather difficult
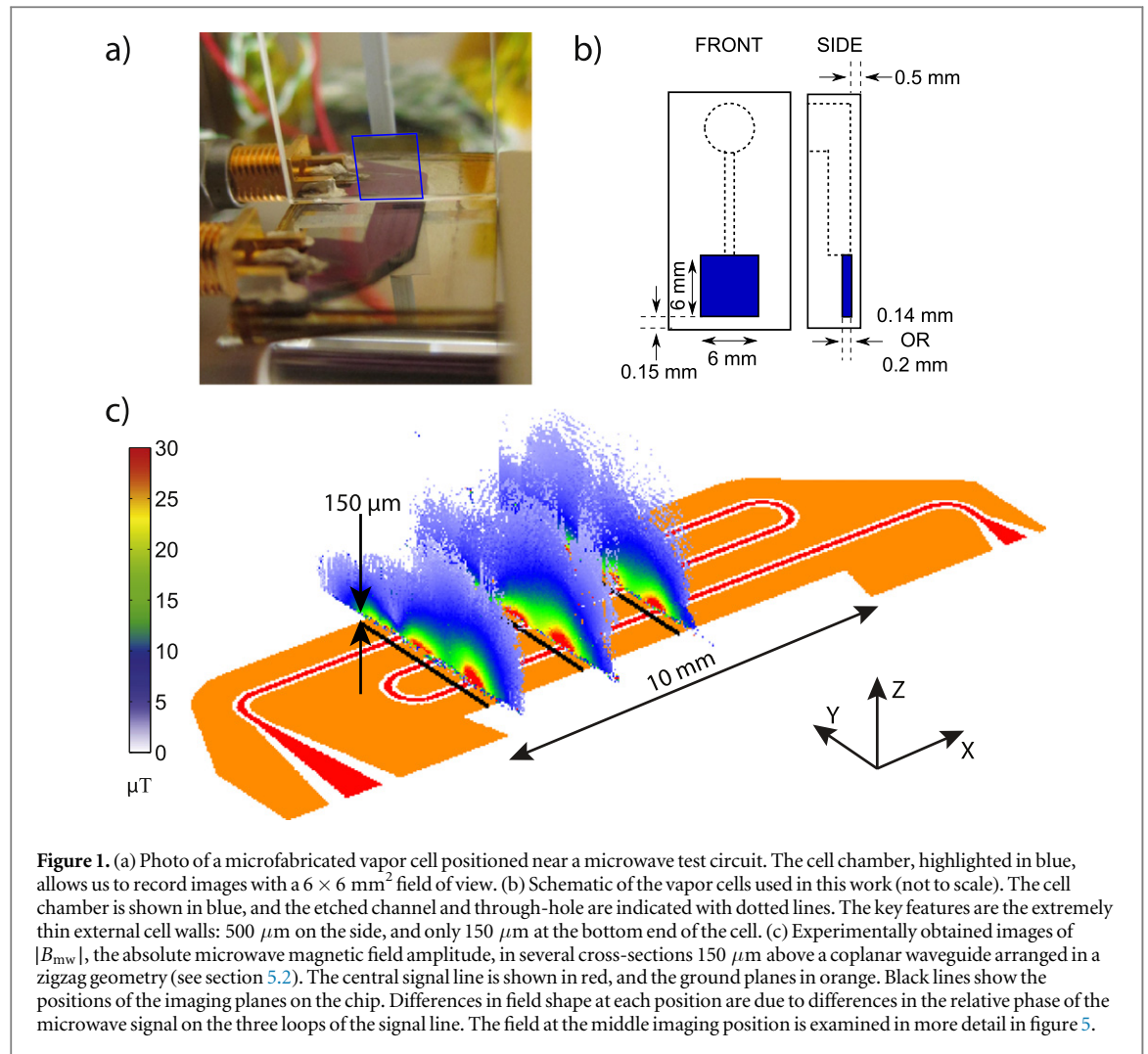
Figure 1. (a) Photo of a microfabricated vapor cell positioned near a microwave test circuit. The cell chamber, highlighted in blue, allows us to record images with a 6×6 mm^2 field of view. (b) Schematic of the vapor cells used in this work (not to scale). The cell chamber is shown in blue, and the etched channel and through-hole are indicated with dotted lines. The key features are the extremely thin external cell walls: 500 μm on the side, and only 150 μm at the bottom end of the cell. (c) Experimentally obtained images of $|B_{\mathrm{mw}}|$, the absolute microwave magnetic field amplitude, in several cross-sections 150 μm above a coplanar waveguide arranged in a zigzag geometry (see section 5.2). The central signal line is shown in red, and the ground planes in orange. Black lines show the positions of the imaging planes on the chip. Differences in field shape at each position are due to differences in the relative phase of the microwave signal on the three loops of the signal line. The field at the middle imaging position is examined in more detail in figure 5.
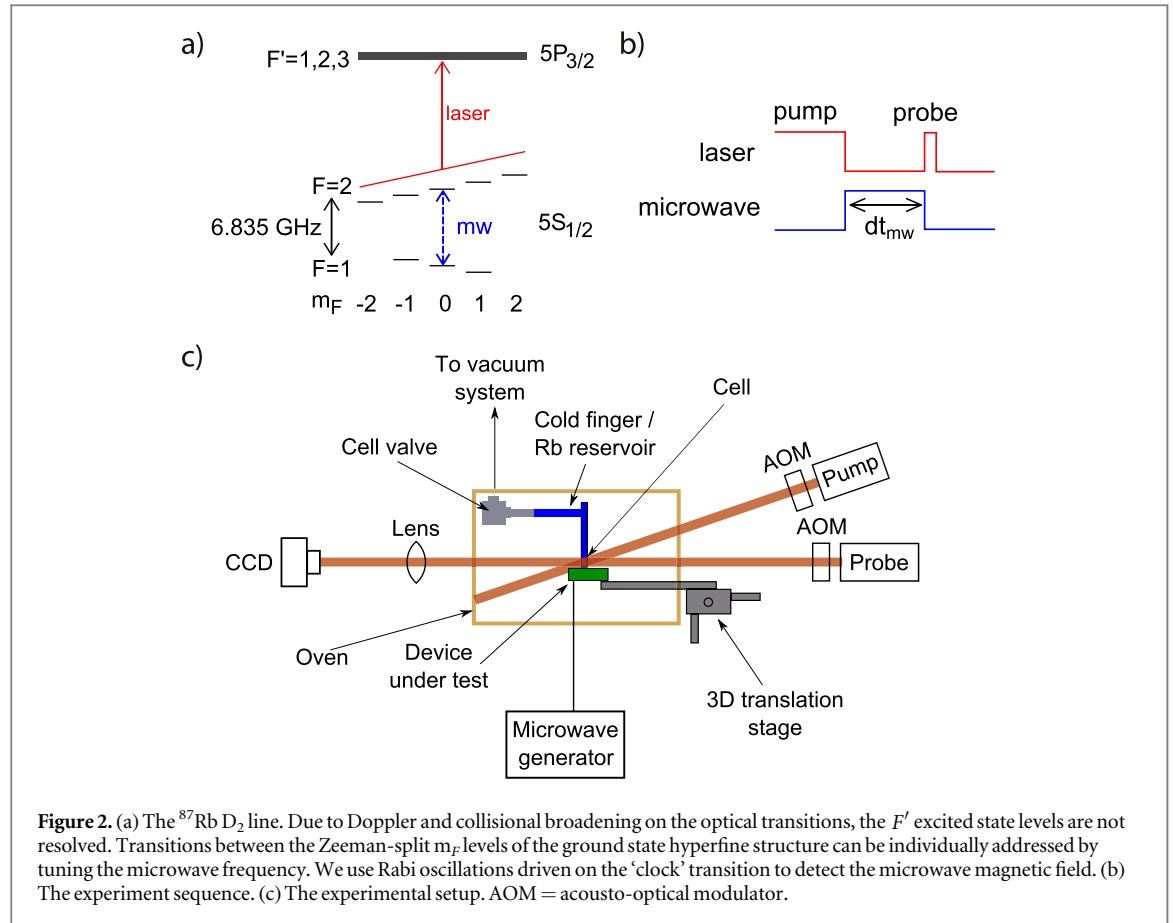
with a scanning probe system. A particularly promising feature of our system is that it can be configured to also image microwave electric fields [13].

Sub-millimeter spatial resolution has been reported in the vapor cell bulk for a number of sensing techniques [9–13, 19–23], but typical outer dimensions of cells have limited usable spatial resolution to the millimeter-scale or larger. Feature sizes in near-fields are on the order of the distance from the field source, meaning that, for example, micrometer-order spatial resolution cannot be exploited when performing sensing millimeters away from a field source. In order to resolve small structures on objects under investigation, it is crucial to measure fields at similarly small distances above the structures. There are many applications where sub-millimeter spatial resolution is essential, such as integrated microwave circuit characterization [24], corrosion monitoring [25–27], and in lab-on-a-chip environments for microfluidic analytical chemistry and bio-sensing [19, 28–30], and molecular imaging [31–33].

We demonstrate our new high-resolution imaging system through the imaging of microwave magnetic near-fields above a selection of microwave circuits. As a demonstration of the flexibility of our setup, we also present vector-resolved images of the dc magnetic field above a wire loop.

2. Imaging microwave magnetic fields in an ultrathin cell

A photograph of our setup and typical microwave field images above a microwave integrated circuit are shown in figure 1. We use a microfabricated glass vapor cell with an inner thickness of 140 μm to position a two-dimensional sheet of atomic rubidium vapor near the microwave device under test (figure 1(a)). The cell features a 150 μm thin side wall (figure 1(b)), which allows us to place the atoms at similarly small distance from the structure. The microwave field of the chip drives Rabi oscillations of frequency $\Omega_{\mathrm{Rabi}}(\vec{r})$ between hyperfine states of the atom, which depend on the projection of the local microwave field vector onto the direction of an applied uniform static magnetic field. The Rabi oscillations are recorded on a camera through the hyperfine

Figure 2. (a) The ^{87}Rb D$_2$ line. Due to Doppler and collisional broadening on the optical transitions, the F' excited state levels are not resolved. Transitions between the Zeeman-split m$_F$ levels of the ground state hyperfine structure can be individually addressed by tuning the microwave frequency. We use Rabi oscillations driven on the 'clock' transition to detect the microwave magnetic field. (b) The experiment sequence. (c) The experimental setup. AOM = acousto-optical modulator.
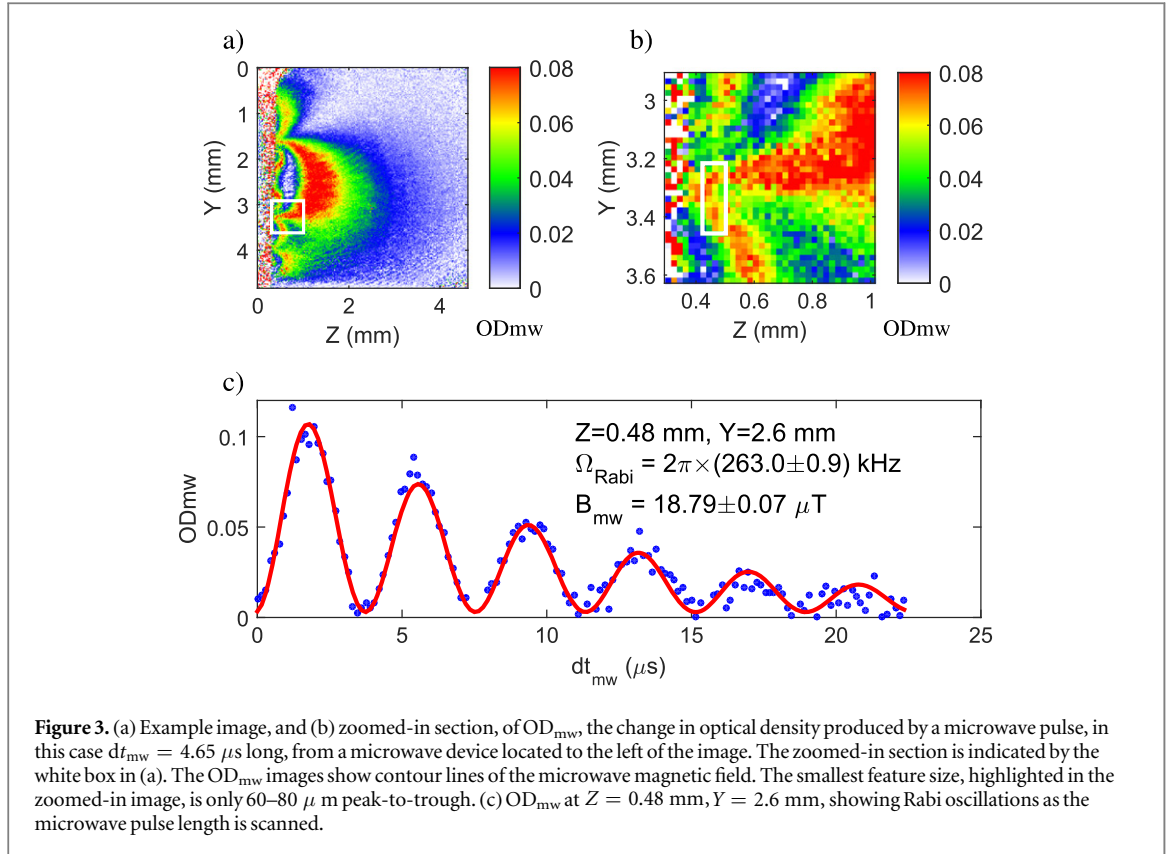
state-dependent absorption of a laser by the atomic vapor. Microwave field images obtained from the observed $\Omega_{\text{Rabi}}(\vec{r})$ are shown in figure 1(c) in several cross-sections of the chip.

A critical component in this work was the design of the two vapor cells used. The cells, identical in all but internal cell thickness, consist of two optically bonded 0.5 and 1.5 $\times$ 20 $\times$ 90 mm pieces of Suprasil glass. As shown schematically in figure 1(b), a cell chamber with a thickness of either 140 μm or 200 μm is etched into one end of the 1.5 mm thick piece. An etched channel connects the cell chamber to a through-hole, around which we attach a glass-to-metal transition with epoxy (Epotek-377). The key advance of our cells is their thin external walls (see figure 1(b)), as thin as 150 μm. In contrast to typical millimeter-scale vapor cell wall thicknesses, our thin walls allow us to image microwave near fields as close as 150 μm above microwave devices, and for the first time take practical advantage of our high spatial resolution.

We fill the cells with a 3:1 mixture of Kr and N$_2$ buffer gasses, with a typical filling pressure of 100 mbar measured at $T_{\text{fill}} = 22$ °C. The heavy Kr acts to localize the Rb atoms, improving our spatial resolution and limiting depolarizing Rb collisions with the cell walls [34]. The N$_2$ gas is included for quenching effects [35, 36].

A schematic of our cell is shown in figure 2(c). The cell and microwave device are placed inside an oven, with operating temperatures of 130 °C to 140 °C chosen to give an optical depth of $OD \approx 1$ [37–39]. The Rb vapor density is controlled by a cold finger wrapped around the end of the glass-to-metal transition, and the 10 °C temperature gradient between the cold finger and the cell helps reduce the deposition rate of Rb and other contaminants on the cell windows. The experiment is surrounded by a cage of Helmholtz coils, which cancel the Earth's magnetic field, and provide a static field of 1–2 G along the X-, Y-, or Z-axes. This field serves as the quantization axis, and the resulting $\sim$MHz Zeeman splitting of the ^{87}Rb hyperfine ground state transitions allows each transition to be individually addressed by tuning the microwave frequency.

Figure 2(a) shows the hyperfine structure of the D$_2$ line of ^{87}Rb and the relevant microwave and optical transitions involved. We produce images of each of the polarization components of the microwave magnetic field, using Rabi oscillations driven on the $|F = 1, m_F = 0\rangle \rightarrow |F = 2, m_F = 0\rangle$ 'clock' transition of the ^{87}Rb hyperfine ground state [8–10]. The Rabi frequency on this transition is given by $\Omega_{\text{Rabi}}(\vec{r}) = \frac{\mu_B}{\hbar} B_{\text{mw}}(\vec{r})$, where $B_{\text{mw}}(\vec{r}) = (\vec{B}_{\text{mw}}(\vec{r}) \cdot \vec{B})/|\vec{B}|$ is the projection of the local microwave field vector $\vec{B}_{\text{mw}}(\vec{r})$ onto the direction of an applied uniform static magnetic field $\vec{B}$. Imaging with the static field pointing in the X-, Y-, and Z-directions allows us to image each polarization component in turn. Using atoms as sensors, our technique avoids the

Figure 3. (a) Example image, and (b) zoomed-in section, of OD_{mw}, the change in optical density produced by a microwave pulse, in this case $dt_{mw} = 4.65\ \mu s$ long, from a microwave device located to the left of the image. The zoomed-in section is indicated by the white box in (a). The OD_{mw} images show contour lines of the microwave magnetic field. The smallest feature size, highlighted in the zoomed-in image, is only 60–80 μ m peak-to-trough. (c) OD_{mw} at $Z = 0.48\ mm$, $Y = 2.6\ mm$, showing Rabi oscillations as the microwave pulse length is scanned.

significant calibration problem in other microwave sensors [40], relating the field to a measured oscillation frequency and well-known fundamental physical constants. Data taking is fast, due to the parallel nature of the measurement (imaging as opposed to scanning). By applying an external static magnetic field, we have imaged microwave fields from 2.3 to 26.4 GHz with a single device [41]. The technique is applicable to microwave devices of all types, recently showing success in characterizing and debugging microwave cavities in high-performance miniaturized atomic clocks [10, 42, 43].

We begin an experiment sequence, shown in figure 2(b), by preparing the atoms in the ^{87}Rb $F = 1$ ground state with a 1 ms optical pumping pulse. Through frequent ($\sim 10^9\ s^{-1}$) collisions with the buffer gas, Rb atoms sample the entire velocity space over the course of the optical pumping pulse (and also the subsequent probe pulse). We typically see a 30% reduction in OD due to optical pumping. The optical pumping efficiency is below 100% due to several factors: radiation trapping, collisional broadening of the optical line, absorption due to ^{85}Rb, and the detuning of the lasers from the collisionally shifted ^{87}Rb and ^{85}Rb optical lines [44]. We drive Rabi oscillations by injecting a microwave pulse of length dt_{mw} into the microwave device under test. We then image the resulting repopulation of the $F = 2$ state with a $dt_{probe} = 0.3\ \mu s$ probe pulse using absorption imaging, which selectively detects the $F = 2$ state [10, 45]. The optical pumping and probing is performed with two separate 780 nm diode lasers, frequency stabilized to the $F = 2 \rightarrow F' = 2$, 3 crossover peak of the ^{87}Rb D$_2$ line, red-shifted by an AOM 80MHz from the stabilization point, and with intensities of 120 mW cm^{-2} and 30 mW cm^{-2}, respectively. The short probe pulse length ensures that optical pumping due to the probe pulse is minimal. We take reference images to account for short and long term drifts, and combine the images to give an image of OD_{mw}, the change in optical density (OD) induced by the microwave pulse. An example OD_{mw} image is shown in figure 3(a). The inhomogeneous microwave field drives Rabi oscillations at different rates across the image, which form patterns in OD_{mw} following the contour lines of the microwave field. Atoms along the outermost (mostly) red line of figure 3(a) are at the peak of their first Rabi oscillation, corresponding to maximal repopulation of the absorptive $F = 2$ state. The inner red line corresponds to a region of higher field, where atoms are at the peak of their second oscillation. We take multiple OD_{mw} images, scanning dt_{mw}, to produce OD_{mw} movies. A sample of these movies are available online, with the frame rate matching the 10 Hz image acquisition rate of our experiment. The counter on top of the movies indicates the microwave pulse duration. As shown in figure 3(c), each pixel in these movies has an oscillating signal which we can fit to obtain the local microwave field strength.

3. Spatial resolution

The longitudinal spatial resolution of our imaging setup is set by the 140 or 200 μm thickness of the cell. The buffer gas pressures set a similar transverse spatial resolution, by determining the distance an atom can diffuse over the course of a measurement [34]. At $T = 135\ ^\circ$C, we estimate the r.m.s diffusion distance during a $dt_{mw} = T_1 = 8.8\ \mu$s measurement to be $\Delta x = \sqrt{2D dt_{mw}} = 50\ \mu$m. Here, T_1 is the hyperfine population relaxation time constant in the cell. The diffusion coefficient, D, is given by $1/D = 1/D_{Kr} + 1/D_{N_2}$, where $D_{Kr(N_2)} = D_{0,Kr(N_2)} \frac{P_0}{P_{Kr(N_2)}} (\frac{T}{T_0})^{3/2}$, $P_0 = 1$ atm, $P_{Kr(N_2)}$ is the Kr (N$_2$) pressure, and we have used $D_{0,Kr} = 0.068$ cm^2 s^{-1} [46] and $D_{0,N_2} = 0.159$ cm^2 s^{-1} [47]. These are order-of-magnitude increases in spatial resolution compared to previous imaging experiments [9, 13, 21, 48].

Peak-to-trough feature sizes as small as $70 \pm 10\ \mu$m can be seen in the OD$_{mw}$ images, approaching the estimated diffusion-limited spatial resolution. An example is shown in figure 3.

4. Microwave field sensitivity

The 6×6 mm cell can be thought of as an array of $N_{sens} = 120 \times 120$ sensors, with each sensor corresponding to a 50 μm $\times$ 50 μm $\times$ 140 μm voxel. The sensor size is given by the diffusion-limited spatial resolution, with a sensor volume $V = 1.8 \times 10^{-7}$ cm^3. To estimate our experimental sensitivity, we examined CCD pixels binned in 2×2 blocks, corresponding to an area of $42 \times 42\ \mu$m^2, slightly smaller than the sensor size. The fitting error to our microwave Rabi data was as low as 21 nT per 2×2 pixels, giving an estimated sensitivity of $\delta B_{mw}^{exp} = 1.4\ \mu$T Hz$^{-1/2}$ per sensor, taking into account the 4440 s measurement time (148 averaged runs). Integrating over a larger volume would give an increase in sensitivity, at the expense of spatial resolution.

We record data for all of the sensors in our array simultaneously. Compared to creating an image by scanning a single sensor, this improves our data-taking speed by a factor of at least N_{sens}, or four orders of magnitude. The effective sensitivity is therefore significantly improved by our parallel imaging, and a single, scanned sensor would require a sensitivity of at least $\delta B_{mw}^{exp}/\sqrt{N_{sens}} = 12$ nT Hz$^{-1/2}$ to produce an image with the same sensitivity. Parallel imaging is also more suitable than scanning for applications requiring high temporal resolution over an image.

We can compare our experimental sensitivity with the photon shot noise limited sensitivity. Assuming $\Omega_{Rabi}\ dt_{mw} \ll \pi$, we have [44]

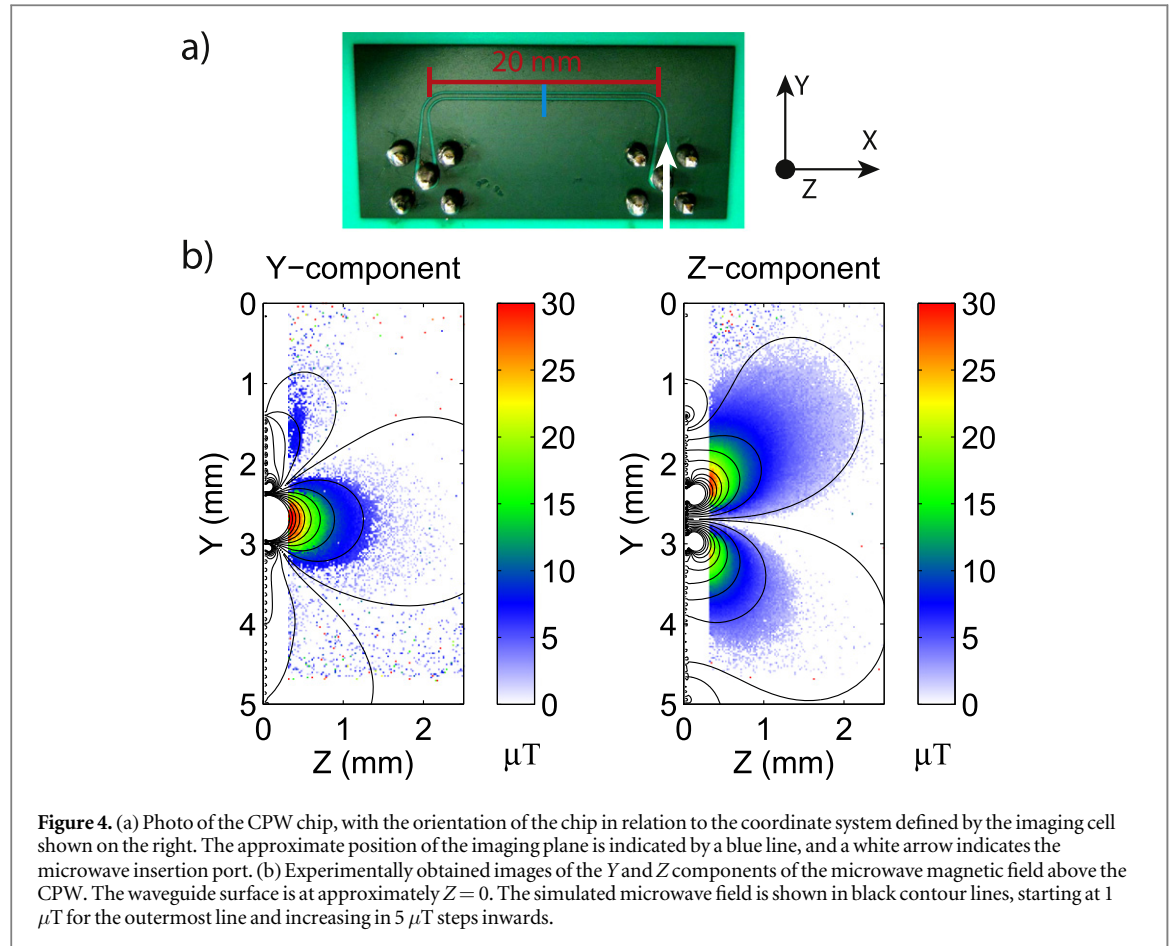$$\delta B_{photon} = \sqrt{\frac{dt_{run}}{N_{shots}}} \frac{2}{dt_{mw}} \frac{\hbar}{\mu_B} \frac{OD_{min}}{OD_{mw}^{max}} \exp\left(dt_{mw}/\tau_2\right). \qquad (1)$$

We first calculate δB_{photon} for conditions matching our experiment parameters: an experiment run of $N_{shots} = 150$ shots taking a time $dt_{run} = 30$ s; $dt_{mw} = 22.5\ \mu$s; an atomic coherence lifetime $\tau_2 = 7.8\ \mu$s; a measured operating temperature of $T_{res} = 140\ ^\circ$C; total buffer gas pressure of $P_{fill} = 100$ mbar; optical pumping resulting in $1/3$ of the atomic population residing in each of the $F = 1$ ground states, such that $OD_{mw}^{max} = \frac{1}{3}OD_{87} = 0.24$, where OD_{87} is the OD of the ^{87}Rb in the cell; and a photon shot noise limited $OD_{min} = \sqrt{2}\ [\ Q\ I_{probe}\ e^{-OD}\ A\ dt_{probe}/(\hbar\omega_L)\ ]^{-1/2} = 1.0 \times 10^{-2}$, where ω_L is the laser frequency, $Q = 0.27$ is the camera quantum efficiency, $I_{probe} = 30$ mW cm^{-2} is the probe intensity, $dt_{probe} = 0.3\ \mu$s is the probe duration, and the 2×2 pixel area is $A = 42 \times 42\ \mu$m^2. This gives us $\delta B_{photon} = 0.45\ \mu$T Hz$^{-1/2}$. The exact operating temperature was unclear, however, with measurements of the OD indicating that the operating temperature may have been closer to $T_{res} = 130\ ^\circ$C, which would give $\delta B_{photon} = 0.28\ \mu$T Hz$^{-1/2}$. We therefore conclude that our measured $\delta B_{mw}^{exp} = 1.4\ \mu$T Hz$^{-1/2}$ is $3-5$ times the photon shot noise limit determined by our experiment parameters. Analysis of OD$_{mw}$ noise in the absence of a microwave field indicates that half of the δB_{mw}^{exp} in excess of δB_{photon} is caused by imaging noise, due to factors such as camera readout noise and fluctuations in the intensities and frequencies of the lasers. Sources for the second half of the excess noise include fitting errors and timing jitter in the experiment sequence. We also note that we perform the imaging without magnetic shielding.

The optimal photon shot noise limited sensitivity, $\delta B_{photon}^{opt} = 0.08\ \mu$T Hz$^{-1/2}$, is reached for $T_{res} = 130\ ^\circ$C, $P_{fill} = 60$ mbar, and with the laser tuned to the buffer-gas-shifted ^{87}Rb $F = 2 \rightarrow F' = 2$ line. Assuming that we can reach the photon shot noise limit, by reducing the excess noise from the above sources, we could expect a factor of 17.5 improvement in sensitivity with only minor modifications to our setup.

An improvement in sensitivity of several orders of magnitude is possible with more involved modifications. We are operating 5×10^5 above the atomic projection noise limit, the ultimate sensitivity limit of an atom-based sensor [2]. Both δB_{mw}^{exp} and δB_{photon} are limited by the camera readout speed and data-saving time, which give a poor experiment duty cycle (10 OD$_{mw}$ images per second) and result in the atoms sitting uninterrogated for the vast majority of the time. This could be dramatically sped up with a different camera and camera operation

Figure 4. (a) Photo of the CPW chip, with the orientation of the chip in relation to the coordinate system defined by the imaging cell shown on the right. The approximate position of the imaging plane is indicated by a blue line, and a white arrow indicates the microwave insertion port. (b) Experimentally obtained images of the *Y* and *Z* components of the microwave magnetic field above the CPW. The waveguide surface is at approximately $Z = 0$. The simulated microwave field is shown in black contour lines, starting at 1 μT for the outermost line and increasing in 5 μT steps inwards.

mode, and we note that 50×50 pixel imaging of ultracold atoms has been reported with a continuous frame rate of 2500 fps [18]. Approaching the atomic projection noise limit will ultimately require moving to a quasi-continuous measurement scheme, likely based on Faraday rotation [18, 49], and perhaps replacing the CCD camera with an array of photodiodes.

## 5. Imaging microwave fields above test structures

In order to characterize and demonstrate our imaging system, we created three demonstration structures. The structures, shown in figures 4 and 5, respectively, are: a coplanar waveguide (CPW); a waveguide making several bends across its substrate, which we dubbed the 'Zigzag' chip; and a split-ring resonator (SRR). All of the microwave field measurements were made using the 140 μm cell.

For imaging, the chip is generally placed perpendicular to the end of the vapor cell, as shown in figure 2(b). For chips built on a transparent or reflective substrate, operation in a second mode is also possible, with the chip placed in front of and parallel to the vapor cell, as shown in figure 6(a).

We use the program Sonnet to perform a simulation of the microwave propagation on our structures using the method of moments. This technique is well suited for our mostly planar structures, excited at a single frequency. The program outputs the current distribution on the chip, from which we compute the magnetic near-fields using the Biot–Savart law. The only free parameters in comparisons with measurement were the amplitude of the input microwave signal and the exact position of the cell relative to the chip.

5.1. The coplanar waveguide

CPWs are a ubiquitous building block of microwave circuits [24], and provide a simple structure which can be readily and robustly compared with simulations. The CPW used in this work, shown in figure 4(a), has a 500 μm wide central signal strip, with 105 μm gaps to ground planes on either side. Figure 4(b) shows images of the *Z*- and *Y*-components of the CPW microwave magnetic field (the very weak *X*-component was not imaged). Simulations of the microwave field are shown as overlaid contour lines. The slight asymmetry is related to the bends in the wires. The good agreement with the simulated field demonstrates the reliability of the imaging technique. Discrepancies may be due to imperfect coupling into the waveguide, and the use of a finite mesh size
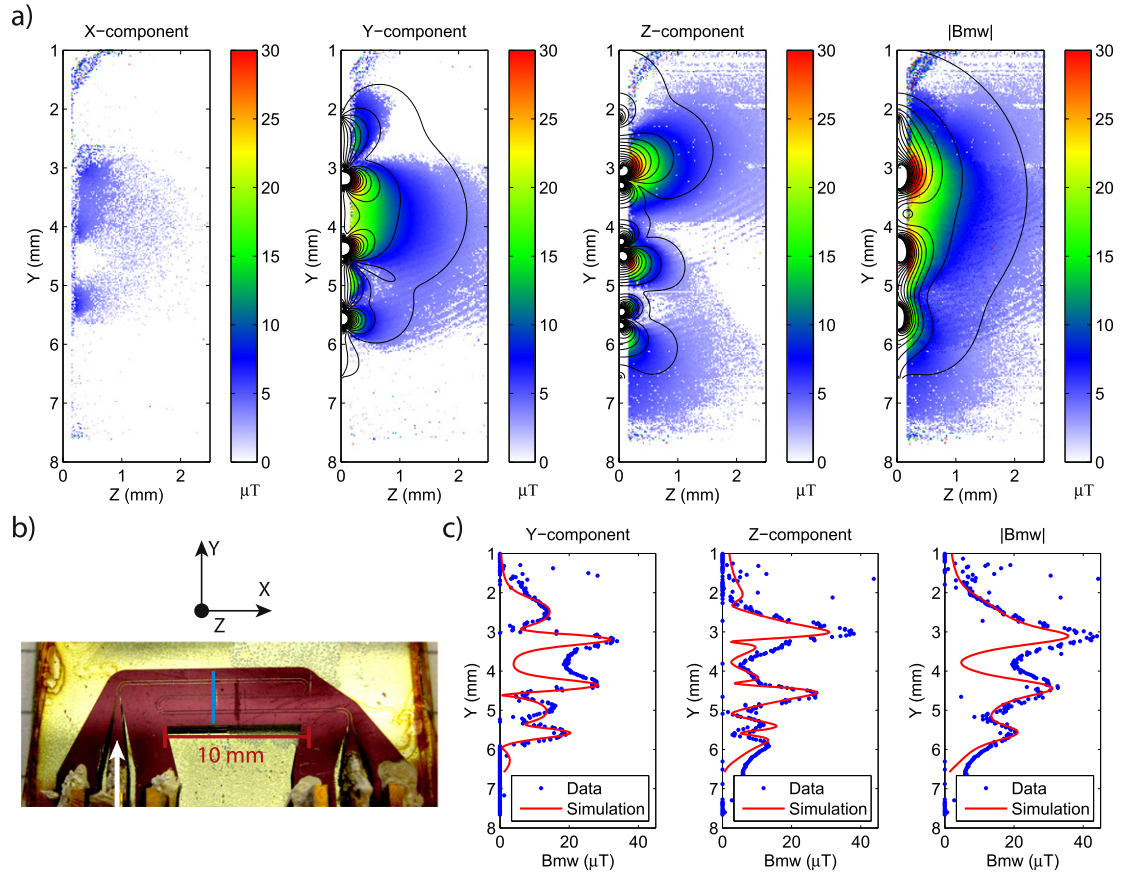
Figure 5. (a) Experimentally obtained images of the *X*-, *Y*-, and *Z*-components of the microwave magnetic field above the Zigzag chip. The magnitude of the microwave field, $|B_{\mathrm{mw}}| = \sqrt{B_X^2 + B_Y^2 + B_Z^2}$, is also shown on the far right. The waveguide surface is at approximately $Z = 0$. The simulated microwave field is shown in black contour lines, starting at 2 μT for the outermost line and increasing in 3 μT steps inwards. (b) Photo of the Zigzag chip. The approximate position of the imaging plane is indicated by a blue line, and a white arrow indicates the microwave insertion port. (c) Cross-sections of the experimentally obtained microwave field (blue dots) approximately 250 μm above the Zigzag chip surface, and comparison to simulation (red lines).
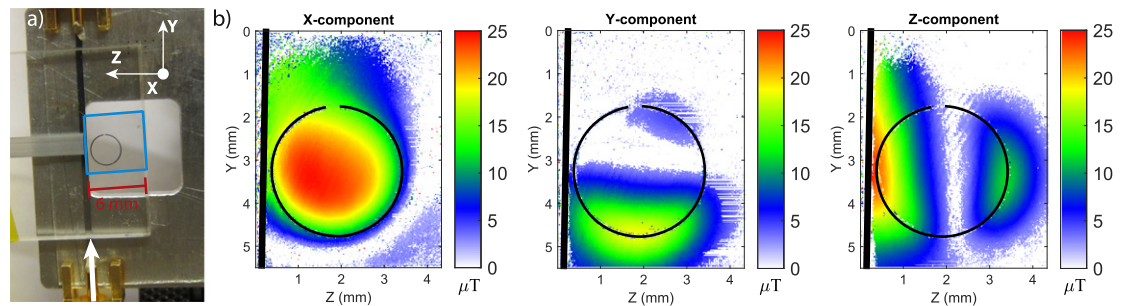
Figure 6. (a) Photo of the SRR chip, demonstrating a second operation mode of the imaging setup, with the glass cell parallel to the transparent chip surface. (b) Experimentally obtained images of the *X*-, *Y*-, and *Z*-components of the microwave magnetic field above the split-ring resonator (SRR). The waveguide surface is parallel to, and a few millimeters in front of, the cell. Black outlines show the positions of the signal line and ring.

for modeling the microwave field through the bends. The images in figure 4(b) demonstrate the importance of thin external vapor cell walls: a vapor cell with standard millimeter-scale external walls would see none of the interesting features.

5.2. The Zigzag chip

The Zigzag chip, shown in figure 5(b), has smaller and more complex features than the CPW, allowing us to highlight the spatial resolution of our setup. The Zigzag waveguide has a 200 μm thick central signal strip, with 50 μm gaps to ground planes either side. The waveguide goes through two bends, resulting in a cross-section in

the imaging plane containing three waveguide sections, each separated by 900 μm. Figure 1 shows quasi-2D slices of the absolute microwave amplitude, $|B_{mw}|$, at three positions above the Zigzag chip. The variation in field shape between the positions is due to the standing wave produced in the waveguide. Figure 5(a) then examines the middle imaging plane of figure 1 (indicated by the blue line in figure 5(b)) in more detail, showing images of each of the polarization components of the microwave field above the chip, which are compared with contour lines from the simulation. Cross-sections of the field near the edge of the vapor cell are shown in figure 5(c). The wide field of view in figures 1 and 5 (>6 mm) was obtained by stitching two sets of images together.

There is general agreement between the measured and simulated fields in figure 5, but not for all features. The amplitude of the simulated X-component of the field is well below the experimental sensitivity, and the measured X-component of the field is likely to be some projection of the Y- and Z-components, caused by imperfect orthogonality between the chip, cell, and coil axes. Additionally, as seen in the cross-sections in figure 5(c), the measured microwave field is much broader than the simulation around $Y = 3$ mm to $Y = 4.5$ mm. Given the spatial resolution shown at $Y = 5.6$ mm, it is reasonable to conclude that this broadening is a real feature of the microwave field. It is unlikely to be due to perturbations induced by the vapor cell, for which we were unable to measure any effect with the Zigzag or CPW chips. Such discrepancies highlight the difficulty of accurately manufacturing and simulating even relatively simple structures such as the Zigzag chip, and the need for direct measurements.

5.3. The split-ring resonator

The SRR chip, shown in figure 6(a), consists of a signal line coupling inductively into a split ring. The split-ring is built on a transparent glass substrate, allowing us to operate in a second mode, with the SRR placed in front of and parallel to the vapor cell. The resonator linewidth was 160 ± 20 MHz, corresponding to a quality factor of 40 ± 5.

The presence of the vapor cell significantly changed the properties of the SRR, by filling the space around the resonator with a glass dielectric. We used this to tune the resonance frequency to match the 6.835 GHz splitting of the ^{87}Rb ground states, adjusting the gap between the cell and the SRR until the resonance was in the desired position. A shift of 1 μm corresponded to a shift in resonance of 5.7 MHz. Note that we were unable to detect any influence of the cell on the CPW or Zigzag chips.

The SRR field is shown in figure 6(b). Like in a solenoid, the SRR field is strongest inside the split-ring, parallel to the split-ring axis in the X-direction. The field then turns outward, seen in the Y- and Z-component images, before returning with a less-dense flux in the X-direction outside the split-ring. The minima in the centers of the Y- and Z-components are due to the field lines traveling out from the field center, and so they cancel out along the central axes. The lopsided nature of the Y-component is due to the presence of the split in the ring.

6. Vector imaging of a DC magnetic field

Our imaging technique can be adapted to measure dc magnetic fields. We use a Ramsey sequence [10], where the single microwave pulse of the above Rabi sequence is replaced by two $\pi/2$ pulses separated by a time dt_{Ramsey}. Driving oscillations on the magnetic field sensitive $|F = 1, m_F = 1\rangle \rightarrow |F = 2, m_F = 1, 2\rangle$ transitions, the oscillation frequency of the Ramsey fringes is equal to the detuning of the microwave from resonance, allowing us to measure the Zeeman shift induced by the applied dc magnetic fields. We can then use the Breit–Rabi formula to obtain the dc field of interest.

To detect individual vector components of a field of interest $\vec{B}$, we apply a second dc magnetic field of strength $C \gg B$. In this way, we are primarily sensitive to the component of $\vec{B}$ that is parallel to $\vec{C}$. For $\vec{C}$ along the X-axis, the measured field, B_{meas}, is [2]

$$B_{meas} = \sqrt{\left(C + B_X\right)^2 + B_Y^2 + B_Z^2} \approx C + B_X. \tag{2}$$

We can obtain C in a separate reference measurement, and subtract this from B_{meas} to obtain B_X. The full vector magnetic field can be obtained by imaging with the C-field applied along each of the X-, Y-, and Z-axes.

Figure 7 shows images of the dc field above a 2 mm diameter wire loop, taken using the 200 μm thick cell. Again, we see a solenoid-like field, with a strong, uniform X-component, and the field turning outwards in the Y- and Z-components. Following the discussion on microwave sensitivity in section 4, fitting uncertainties give a sensitivity as small as $\delta B_{dc}^{exp} = 1.6$ μT Hz$^{-1/2}$ for a $40 \times 40 \times 200$ μm sensor. As discussed in section 4, the dominant limiting factor is our poor experiment duty cycle, the improvement of which promises an increase in sensitivity by several orders of magnitude.
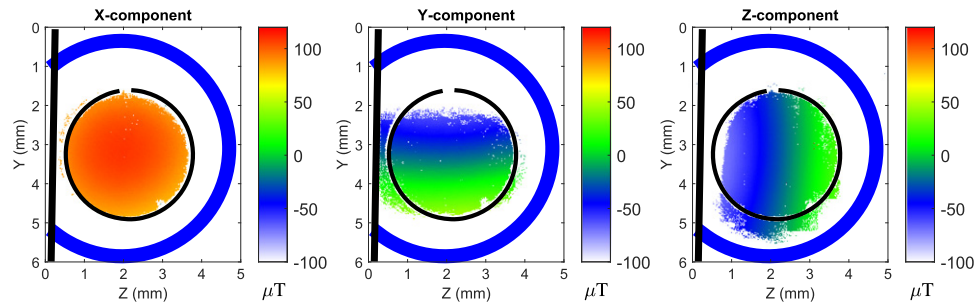
Figure 7. Experimentally obtained images of the *X*-, *Y*-, and *Z*-components of a dc magnetic field X mm above a wire loop. Positive and negative field values represent opposite directions. The field of view corresponds to the *X*-component of the SRR microwave magnetic field, which was used to drive the Ramsey oscillations used to image the dc field. Outlines show the positions of the current loop (blue) and SRR (black). The coordinate system is the same as shown in figure 6(a).

7. Conclusions and outlook

We have demonstrated a new setup for high-resolution imaging of electromagnetic near fields, through the imaging of microwave fields above a variety of microwave devices, and the dc magnetic field above a wire loop. Microwave imaging is performed with a 120×120 array of $50 \times 50 \times 140~\mu\text{m}^3$ sensors, with the sensor size given by atomic diffusion during a measurement and the 140 μm cell thickness. The sensitivity per sensor, $\delta B_{\text{mw}}^{\text{exp}} = 1.4~\mu\text{T Hz}^{-1/2}$, is primarily limited by the experiment duty cycle, and improvements of several orders of magnitude should be achievable. We obtained a similar sensitivity for dc magnetic field imaging in a 200 μm thick cell. The setup allows us to image fields as close as 150 μm above surfaces, resulting in an order of magnitude increase in the resolution of surface features compared to previous vapor cell sensors. To our knowledge, this is the first vapor cell with such thin walls, and it should serve as a model for future vapor cells used in near-field sensing.

We currently perform imaging with the microwave device exposed to temperatures around 140 °C, which would be a barrier to the testing of temperature-sensitive devices. In future setups, we will move to locally heating the vapor cell with a 1.5 μm laser [50], significantly reducing the heat exposure of the device under test. If required, a further reduction in operating temperature could be achieved by using LIAD techniques to modulate the Rb vapor density [51].

Our microwave detection technique is not limited to ^{87}Rb, and can be applied to any system comprised of two states coupled by a microwave transition with optical read-out of the states, including the other alkali atoms, and solid state 'atom-like' systems, such as NV centers [52]. NV center–based imaging systems provide nanoscale resolution and typically work in scanning mode. They are thus complementary to our widefield imaging technique which is well adapted to image features on the micrometer scale with temporal resolution.

The full characterization of a microwave near field requires measurements of both the electric (E_{mw}) and magnetic (B_{mw}) components, as there is no straightforward relationship between the components. Alkali atoms in Rydberg states have proven to be excellent sensors of E_{mw}[11–13], but Rydberg states are quickly destroyed in collisions with buffer gas atoms. The vapor cell requirements for B_{mw} and E_{mw} imaging would therefore seem somewhat incompatible: we require high buffer gas pressures to prevent wall relaxation and provide spatial resolution for B_{mw} imaging, but require that there is little to no buffer gas present for E_{mw} imaging. However, with the addition of a 480 nm laser to excite Rb Rydberg states, our control over the buffer gas inside our ultrathin cells would allow us to perform an E_{mw} measurement without buffer gas, then fill the cell with buffer gas and image B_{mw}. Our setup would therefore be ideal for measurements of both components, and we would avoid the errors that using two different cell would bring, such as in cell alignment.

Microwave sensing and imaging (MSI) is an emerging field that has shown promise in a range of applications, particularly for breast cancer screening [15–17]. Current microwave detection systems consist of an array of microwave antennas sensitive to E_{mw}. Optimal image reconstruction requires a high sensor density; however, the density is limited by cross-talk between antennas, and by their perturbations of the microwave field. Sensor calibration is also a significant concern [17]. Atomic sensors are not affected by any of these problems. Following the success of vapor cell magnetometers in diagnostic imaging of the heart [53, 54] and brain [55–58], microwave imaging with vapor cells may also prove to be an attractive medical tool.

Our spatial resolution, sensitivity and distance of approach are now sufficient for characterizing a range of scientific and industrial microwave devices operating at 6.8 GHz. However, frequency tunability is essential for wider applications, with industry particularly interested in imaging techniques for frequencies above 18 GHz. It is possible to use a large dc magnetic field to Zeeman shift the hyperfine ground state transitions to any desired

frequency, from dc to 100s of GHz. Using a 0.8 T solenoid, we have demonstrated microwave detection up to 26.4 GHz in a proof-of-principle setup, which will be presented in a subsequent paper [41].

Acknowledgments

References

[1] Budker D, Gawlik W, Kimball D F, Rochester S M, Yashchuk V V and Weis A 2002 Resonant nonlinear magneto-optical effects in atoms *Rev. Mod. Phys.* **74** 1153
[2] Budker D and Romalis M 2007 Optical magnetometry *Nat. Phys.* **3** 227–34
[3] Kitching J, Knappe S and Donley E A 2011 Atomic sensors — a review *IEEE Sensors J.* **11** 1749–58
[4] Kominis I K, Kornack T W, Allred J C and Romalis M V 2003 A subfemtotesla multichannel atomic magnetometer *Nature* **422** 596–9
[5] Dang H B, Maloof A C and Romalis M V 2010 Ultrahigh sensitivity magnetic field and magnetization measurements with an atomic magnetometer *Appl. Phys. Lett.* **97** 151110
[6] Savukov I, Seltzer S, Romalis M and Sauer K 2005 Tunable atomic magnetometer for detection of radio-frequency magnetic fields *Phys. Rev. Lett.* **95** 063004
[7] Savukov I, Karaulanov T and Boshier M G 2014 Ultra-sensitive high-density Rb-87 radio-frequency magnetometer *Appl. Phys. Lett.* **104** 023504
[8] Böhi P, Riedel M F, Hänsch T W and Treutlein P 2010 Imaging of microwave fields using ultracold atoms *Appl. Phys. Lett.* **97** 051101
[9] Böhi P and Treutlein P 2012 Simple microwave field imaging technique using hot atomic vapor cells *Appl. Phys. Lett.* **101** 181107
[10] Horsley A, Du G-X, Pellaton M, Affolderbach C, Mileti G and Treutlein P 2013 Imaging of relaxation times and microwave field strength in a microfabricated vapor cell *Phys. Rev.* A **88** 063407
[11] Sedlacek J A, Schwettmann A, Kübler H, Löw R, Pfau T and Shaffer J P 2012 Microwave electrometry with Rydberg atoms in a vapor cell using bright atomic resonances *Nat. Phys.* **8** 819–24
[12] Sedlacek J, Schwettmann A, Kübler H and Shaffer J P 2013 Atom based vector microwave electrometry using rubidium Rydberg atoms in a vapor cell *Phys. Rev. Lett.* **111** 063001
[13] Fan H Q, Kumar S, Daschner R, Kübler H and Shaffer J P 2014 Subwavelength microwave electric-field imaging using Rydberg atoms inside atomic vapor cells *Opt. Lett.* **39** 3030–3
[14] Fan H, Kumar S, Sedlacek J, Kübler H, Karimkashi S and Shaffer J P 2015 Atom based RF electric field sensing *J. Phys. B: At. Mol. Opt. Phys.* **48** 202001
[15] Fear E C, Hagness S C, Meaney P M, Okoniewski M and Stuchly M A 2002 Enhancing breast tumor detection with near-field imaging *IEEE Microwave Mag.* **3** 48–56
[16] Nikolova N 2011 Microwave imaging for breast cancer *IEEE Microwave Mag.* **12** 78–94
[17] Chandra R, Zhou H, Balasingham I and Narayanan R M 2015 On the opportunities and challenges in microwave medical sensing and imaging *IEEE Trans. Biomed. Eng.* **62** 1667–82
[18] Gajdacz M, Pedersen P L, Mørch T, Hilliard A J, Arlt J and Sherson J F 2013 Non-destructive faraday imaging of dynamically controlled ultracold atoms *Rev. Sci. Instrum.* **84** 083105
[19] Xu S, Crawford C, Rochester S, Yashchuk V, Budker D and Pines A 2008 Submillimeter-resolution magnetic resonance imaging at the Earth's magnetic field with an atomic magnetometer *Phys. Rev.* A **78** 013404
[20] Zhao K F and Wu Z 2008 Evanescent wave magnetometers with ultrathin ($\sim 100~\mu$m) cells *Appl. Phys. Lett.* **93** 101101
[21] Fescenko I and Weis A 2014 Imaging magnetic scalar potentials by laser-induced fluorescence from bright and dark atoms *J. Phys. D: Appl. Phys.* **47** 235001
[22] Hakhumyan G, Leroy C, Pashayan-Leroy Y, Sarkisyan D and Auzinsh M 2011 High-spatial-resolution monitoring of strong magnetic field using Rb vapor nanometric-thin cell *Opti. Commun.* **284** 4007–12
[23] Sargsyan A, Tonoyan A, Mirzoyan R, Sarkisyan D, Wojciechowski A M, Stabrawa A and Gawlik W 2014 Saturated-absorption spectroscopy revisited: Atomic transitions in strong magnetic fields (>20 mT) with a micrometer-thin cell *Opt. Lett.* **39** 2270
[24] Wolff I 2006 *Coplanar Microwave Integrated Circuits* (New York: Wiley)
[25] Juzeliunas E 2006 Advances in detection of magnetic fields induced by electrochemical reactions: a review *J. Solid State Electrochem.* **11** 791–8
[26] Gallo G E, Popovics J S and Chapman P L 2011 Corrosion monitoring of metals *Eur. J. Environ. Civil Eng.* **15** 633–47
[27] Gallo G E and Popovics J S 2012 Monitoring active corrosion of metals in natural environments with magnetometry *Corros. Sci.* **63** 1–4
[28] Xu S, Rochester S M, Yashchuk V V, Donaldson M H and Budker D 2006 Construction and applications of an atomic magnetic gradiometer based on nonlinear magneto-optical rotation *Rev. Sci. Instrum.* **77** 083106
[29] Xu S, Yashchuk V V, Donaldson M H, Rochester S M, Budker D and Pines A 2006 Magnetic resonance imaging with an optical atomic magnetometer *Proc. Natl. Acad. Sci. USA* **103** 12668–71
[30] Harel E, Schröder L and Xu S 2008 Novel detection schemes of nuclear magnetic resonance and magnetic resonance imaging: Applications from analytical chemistry to molecular sensors *Annu. Rev. Anal. Chem.* **1** 133–63
[31] Yao L, Jamison A C and Xu S 2010 Scanning imaging of magnetic nanoparticles for quantitative molecular imaging *Angew. Chem. Int. Ed.* **49** 7493–6
[32] Yu D, Ruangchaithaweesuk S, Yao L and Xu S 2012 Detecting molecules and cells labeled with magnetic particles using an atomic magnetometer *J. Nanopart. Res.* **14** 1135
[33] Yao L, Wang Y and Xu S 2013 Label-free microRNA detection based on exchange-induced remnant magnetization *Chem. Commun.* **49** 5183–5
[34] Vanier J, Audoin C and Hilger A 1989 *The Quantum Physics of Atomic Frequency Standards* vol 1 (Bristol: Adam Hilger)
[35] Chevrollier M 2012 Radiation trapping and Lévy flights in atomic vapors: An introductory review *Contemp. Phys.* **53** 227–39
[36] Rosenberry M, Reyes J, Tupa D and Gay T 2007 Radiation trapping in rubidium optical pumping at low buffer-gas pressures *Phys. Rev.* A **75** 023401

[37] Siddons P, Adams C S, Ge C and Hughes I G 2008 Absolute absorption on rubidium D lines: comparison between theory and experiment *J. Phys. B: At. Mol. Opt. Phys.* **41** 155004

[38] Weller L, Bettles R J, Siddons P, Adams C S and Hughes I G 2011 Absolute absorption on the rubidium D1 line including resonant dipole-dipole interactions *J. Phys. B: At. Mol. Opt. Phys.* **44** 195006

[39] Zentile M A, Andrews R, Weller L, Knappe S, Adams C S and Hughes I G 2014 The hyperfine paschen-back faraday effect *J. Phys. B: At. Mol. Opt. Phys.* **47** 075005

[40] Zelder T, Geck B, Rolfes I and Eul H 2008 Radio science contactless vector network analysis with varying transmission line geometries *Adv. Radio Sci.* **6** 19–25

[41] Horsley A and Treutlein P 2015 in preparation

[42] Ivanov A, Bandi T, Du G-X, Horsley A, Affolderbach C, Treutlein P, Mileti G and Skrivervik A K 2014 Experimental and numerical studies of the microwave field distribution in a compact magnetron-type microwave cavity *Proc. of the 28th European Frequency and Time Forum (EFTF) (June 22–26 2014)* (Switzerland: Neuchatel)

[43] Affolderbach C, Du G-X, Bandi T, Horsley A, Treutlein P and Mileti G 2015 Imaging microwave and DC magnetic fields in a vapor-cell Rb atomic clock *IEEE Trans. Instrum. Meas.* **99**

[44] Horsley A 2015 High resolution field imaging with atomic vapor cells *PhD Thesis* Department of Physics, University of Basel, Switzerland

[45] Horsley A, Du G-X, Pellaton M, Affolderbach C, Mileti G and Treutlein P 2013 Spatially resolved measurement of relaxation times in a microfabricated vapor cell *Proc. of the 2013 Joint IEEE-UFFC, EFTF and PFM Symp.* 575–8

[46] Chrapkiewicz R, Wasilewski W and Radzewicz C 2014 How to measure diffusional decoherence in multimode rubidium vapor memories? *Opt. Commun.* **317** 1–6

[47] Ishikawa K and Yabuzaki T 2000 Diffusion coefficient and sublevel coherence of Rb atoms in N_2 buffer gas *Phys. Rev.* A **62** 065401

[48] Mikhailov E E, Novikova I, Havey M D and Narducci F A 2009 Magnetic field imaging with atomic Rb vapor *Opt. Lett.* **34** 3529–31

[49] Allred J, Lyman R, Kornack T and Romalis M 2002 High-sensitivity atomic magnetometer unaffected by spin-exchange relaxation *Phys. Rev. Lett.* **89** 130801

[50] Mhaskar R, Knappe S and Kitching J 2012 A low-power, high-sensitivity micromachined optical magnetometer *Appl. Phys. Lett.* **101** 5–8

[51] Marmugi L, Gozzini S, Lucchesini A, Bogi A, Burchianti A and Marinelli C 2012 All-optical vapor density control for electromagnetically induced transparency *J. Opt. Soc. Am.* B **29** 2729

[52] Appel P, Ganzhorn M, Neu E and Maletinsky P 2015 Nanoscale microwave imaging with a single electron spin in diamond *New J. Phys.* **17** 112001

[53] Bison G, Castagna N, Hofer A, Knowles P, Schenker J-L, Kasprzak M, Saudan H and Weis A 2009 A room temperature 19-channel magnetic field mapping device for cardiac signals *Appl. Phys. Lett.* **95** 173701

[54] Alem O, Sander T H, Mhaskar R, LeBlanc J, Eswaran H, Steinhoff U, Okada Y, Kitching J, Trahms L and Knappe S 2015 Fetal magnetocardiography measurements with an array of microfabricated optically pumped magnetometers *Phys. Med. Biol.* **60** 4797–811

[55] Savukov I and Karaulanov T 2013 Magnetic-resonance imaging of the human brain with an atomic magnetometer *Appl. Phys. Lett.* **103** 43703

[56] Johnson C N, Schwindt P D D and Weisend M 2013 Multi-sensor magnetoencephalography with atomic magnetometers *Phys. Med. Biol.* **58** 6065–77

[57] Wyllie R, Kauer M, Wakai R T and Walker T G 2012 Optical magnetometer array for fetal magnetocardiography *Opt. Lett.* **37** 2247–9

[58] Shah V K and Wakai R T 2013 A compact, high performance atomic magnetometer for biomedical applications *Phys. Med. Biol.* **58** 8153–61